



HAL
open science

Cyclostratigraphy of the Late Miocene to Pliocene sediments at IODP sites U1425 and U1430 in the Japan Sea and paleoceanographic implications

Shunsuke Kurokawa, Ryuji Tada, Kenji M Matsuzaki, Tomohisa Irino,
Johanna Lofi

► **To cite this version:**

Shunsuke Kurokawa, Ryuji Tada, Kenji M Matsuzaki, Tomohisa Irino, Johanna Lofi. Cyclostratigraphy of the Late Miocene to Pliocene sediments at IODP sites U1425 and U1430 in the Japan Sea and paleoceanographic implications. *Progress in Earth and Planetary Science*, 2019, 6 (1), pp.2. 10.1186/s40645-018-0250-1 . hal-02083020

HAL Id: hal-02083020

<https://hal.umontpellier.fr/hal-02083020>

Submitted on 28 Mar 2019

HAL is a multi-disciplinary open access archive for the deposit and dissemination of scientific research documents, whether they are published or not. The documents may come from teaching and research institutions in France or abroad, or from public or private research centers.

L'archive ouverte pluridisciplinaire **HAL**, est destinée au dépôt et à la diffusion de documents scientifiques de niveau recherche, publiés ou non, émanant des établissements d'enseignement et de recherche français ou étrangers, des laboratoires publics ou privés.

RESEARCH ARTICLE

Open Access



Cyclostratigraphy of the Late Miocene to Pliocene sediments at IODP sites U1425 and U1430 in the Japan Sea and paleoceanographic implications

Shunsuke Kurokawa¹, Ryuji Tada¹, Kenji M. Matsuzaki^{1,2*}, Tomohisa Irino³ and Lofi Johanna⁴

Abstract

High-resolution studies of sedimentary sequences have reconstructed paleoceanographic changes in the Atlantic and southern and equatorial Pacific Oceans during the Late Miocene and Pliocene, but comparable analyses are lacking for the North Pacific Ocean. However, continuous samples of hemipelagic sequences covering this time interval were obtained at Integrated Ocean Drilling Program sites U1425 and U1430 in the Japan Sea during expedition 346. Because the paleoceanography of the Japan Sea was sensitive to glacio-eustatic sea-level changes, changes in the sediment record are manifested as cyclic lithological changes. By using a gamma ray attenuation (GRA) density, which reflects biogenic silica content, as an indicator of sea-level changes, we developed an independent orbitally tuned chronology at each site to construct high-resolution, high-precision age models for the time span of 11.8 to 1.45 Ma. First, the 405-kyr-filtered GRA profile at each site was tuned to 405-kyr-filtered orbital eccentricity. Then, using the 405-kyr-tuned age model, the 100-kyr-filtered GRA profile was tuned to short-eccentricity cycles to adjust the 405-kyr-tuned age models. We used the resulting age models to revise the time intervals of previously published lithological units and paleoceanographic stages for the Japan Sea. Our profiles based on physical properties are a good match to the oxygen isotope record, except for 6.6–3.6 Ma, a time interval with small-amplitude fluctuations in the oxygen isotope record.

Keywords: IODP, Japan Sea, U1425, U1430, Pliocene, Late Miocene, Orbital tuning, Sea level

Introduction

The Late Miocene to Pliocene time encompassed the expansion and stabilization of the East Antarctic ice sheet, the onset of northern hemisphere glaciation and the intensification of the Asian Monsoon system (e.g., Zachos et al. 2001; De Vleeschouwer et al. 2017, Tada et al. 2016; Betzler et al. 2018; Clift 2017; Holbourn et al. 2018). Paleoceanographic changes during this period have been reconstructed at high resolution on the basis of deep-sea sediments mainly from the Atlantic and southern and equatorial Pacific oceans (e.g., Bell et al.

2014, 2015; Westerhold et al. 2005; Holbourn et al. 2005, 2007, 2013a, 2013b, 2018; Drury et al. 2016). This research has shown that changes in Miocene and Pliocene climate and oceanography were closely associated with orbital-scale changes in ice volume and the carbon cycle (Holbourn et al. 2013a, 2013b, 2018; Drury et al. 2016). However, there are few continuous, long-term sedimentary sequences of this age suitable for high-resolution analyses from the northwest Pacific Ocean because the calcium carbonate compensation depth was shallow in the area at that time (e.g., Berger 1967; Berger et al. 1982). For that reason, paleoceanographic conditions of the Pacific Ocean during this period are not well understood.

The Japan Sea has been a semi-enclosed marginal sea since at least the Early Miocene (Iijima and Tada 1990). Its connection to the Pacific Ocean through relatively

* Correspondence: km.matsuzaki@aori.u-tokyo.ac.jp

¹Department of Earth and Planetary Science, Graduate School of Science, The University of Tokyo, 7-3-1 Hongo, Bunkyo-ku, Tokyo 113-0033, Japan

²Present Address Atmosphere and Ocean Research Institute, The University of Tokyo, 5-1-5 Kashiwanoha, Kashiwa, Chiba 277-8564, Japan
Full list of author information is available at the end of the article

shallow straits has made the Japan Sea sensitive to glacio-eustatic sea-level changes, which are manifested as cyclic lithological changes in its sedimentary records (Tada 1994). Therefore, it appears feasible to construct a high-resolution and high-precision age model by the use of cyclostratigraphy based on lithological variations, as inferred from gamma ray data, in hemipelagic sediments from the Japan Sea.

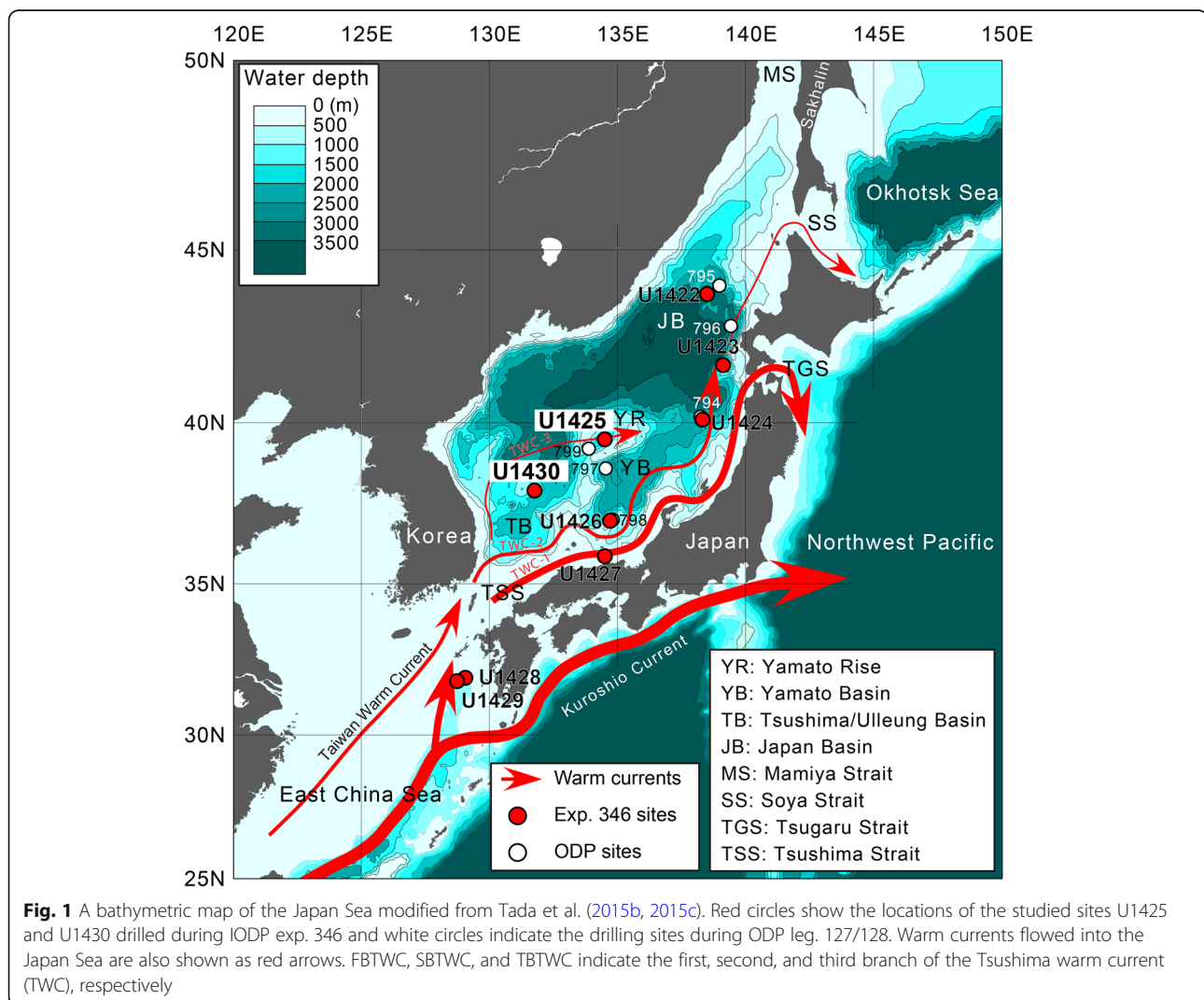
In this study, we constructed an orbitally tuned age model for the hemipelagic sediments of the Japan Sea during the period 11.8–1.45 Ma, reconstructed temporal changes in the physical properties of cores, and compared them with global and regional benthic oxygen isotope records. We utilized core data from Integrated Ocean Drilling Program (IODP) sites U1425 and U1430 in the central and south-central Japan Sea, recovered during expedition 346 (Tada et al. 2015b, 2015c). We used a revised version of the stratigraphic record derived from the cores at each site (Irina et al. 2018) combined

with both shipboard and newly published biostratigraphic data (Kamikuri et al. 2017) to construct high-resolution, high-precision age models at the two sites.

Physical properties measured at high resolution during the cruise were utilized to correlate the sediment records between holes and between coring sites. These physical properties were also used to support orbital tuning because sedimentary cycles were clearly evident in the high-resolution record (e.g., Lourens et al. 2005; Tian et al. 2008).

Oceanographic and geological setting

The Japan Sea, with an area exceeding 10^6 km² and a mean depth of 1667 m, is connected to neighboring seas and the Pacific Ocean through narrow and shallow straits (Fig. 1). The Tsushima Warm Current (TWC), the only current flowing into the sea, controls its oceanographic conditions (Gamo et al. 2014). The TWC



splits into three branches as it enters the Japan Sea (Hase et al. 1999). The first branch originates in the eastern channel of Tsushima Strait and flows along the west coast of Honshu Island. The second branch originates in the western channel of Tsushima Strait and flows initially along the southern Korean Peninsula, then along the shelf edge to the west of and generally parallel to the first branch. However, this branch is also strongly influenced by eddies generated by baroclinic instability (Hase et al. 1999). The third branch originates in the western channel of Tsushima Strait, flows northward along the Korean Peninsula, and then turns to the east around 36° N and forms the Subpolar Front (Kim and Yoon 1999). In the northwestern Japan Sea, cooling and freezing caused by the winter monsoon increases the subsurface water density (Talley et al. 2003), which forms the deep Japan Sea Proper Water, characterized by its high dissolved oxygen content (Gamo et al. 1986). However, oceanographic conditions have been significantly different in the past, and the sediments of the Japan Sea give evidence of the basin's strong sensitivity to regional and global climatic and oceanographic changes (Tada 1994).

The Japan Sea first opened approximately 28 Ma, and the deposition of hemipelagic sediments began around 20 Ma (Tamaki et al. 1992; Tada 1994). In their revised lithostratigraphy of Japan Sea hemipelagic sediments obtained during Ocean Drilling Program (ODP) leg 127, Tada and Iijima (1992) divided the middle Miocene to Holocene sedimentary sequence into six lithological units. Of these, unit 4 (15.5–10.5 Ma) is composed of gray, highly siliceous rocks and has two subdivisions. Subunit 4B (15.5–14 Ma) is composed of claystone with occasional parallel laminations and flattened horizontal burrows, and subunit 4A (14–10.5 Ma) consists of alternating decimeter-scale layers of dark chert and light claystone, the claystone being more strongly bioturbated than the chert. Unit 3 (10.5–6 Ma) is characterized by alternating decimeter-scale layers of non-bioturbated dark diatomaceous silty clay and bioturbated light silty clay. Unit 2 (6–2.5 Ma) is composed of heavily bioturbated, homogeneous greenish diatom ooze and diatomaceous clay. Unit 1 (2.5–0 Ma) is composed of alternating centimeter- to meter-scale layers of dark and light clay to silty clay that are biosiliceous or biocalcareous to various degrees (Tada and Iijima 1992; Tada 1994).

Tada (1994) reconstructed the circulation of the paleo-Japan Sea from oceanographic information (surface and bottom water conditions, calcium carbonate compensation depth, surface productivity, channel position, and sill depth) and divided the evolution of the Japan Sea into five stages corresponding to the deposition of the five uppermost lithological units of Tada and Iijima (1992). During stages 2 and 3 (15.5–6.5 Ma),

which correspond to the deposition of units 4 and 3, respectively, the surface water was predominantly cool and the deep water fluctuated between suboxic and anoxic (Tada 1991, 1994). Tada (1991) interpreted cyclic meter-scale lithological changes and apparently annual parallel laminations in the Onnagawa Formation in northeastern Honshu (equivalent to subunit 4A) to argue that terrigenous input fluctuated periodically due to orbitally driven sea-level oscillations. During stage 4 (6.5–2.5 Ma), corresponding to the deposition of unit 2, cold and oxic surface water flowed into the Japan Sea from the north and formed deep water. The consequent upwelling resulted in higher productivity in the surface water and greater deposition of biogenic silica. Stage 5 (2.5–0 Ma), corresponding to the deposition of unit 1, was characterized by large and frequent oscillations of oceanographic conditions. During interglacial sea-level highstands, the TWC was strong and resulted in the production of deep water within the Japan Sea, such that the bottom water became hyperoxic. During glacial lowstands, the Japan Sea became isolated and the TWC was restricted, leading to density stratification beneath the low-salinity surface water and the development of euxinic bottom water (Tada 1994).

Methods/Experimental

Sites and materials

IODP site U1425 (39°29.44' N, 134°26.55' E, water depth 1909 m) is on a terrace in a northeast-southwest-oriented graben in the middle of Yamato Bank, and site U1430 (37°54.16' N, 131°32.25' E, water depth 1072 m) is about 300 km to the southwest on the southern upper slope of the eastern South Korean Plateau (Tada et al. 2015a, 2015c) (Fig. 1). The location of site U1425 is now under the influence of the third branch of the TWC at the Subpolar Front, and site U1430 is slightly south of the Subpolar Front (Hase et al. 1999). Miocene sediments were recovered at these two sites during expedition 346 (Tada et al. 2015b, 2015c).

The sedimentary sequence at site U1425 covers the time interval from the Late Miocene to the Holocene (Fig. 2a) without any obvious hiatus and is dominated by clay, silty clay, diatomaceous ooze, and siliceous claystone (Tada et al. 2015b). The sequence has been divided into three lithological units (units I to III) on the basis of sediment composition, in particular, the abundance of biosiliceous material (Tada et al. 2015a). At site U1430, the sedimentary sequence extends from the middle Miocene to the Holocene (Fig. 2b) and has been divided into lithological units I to IV (Tada et al. 2015c). Between 7 Ma and approximately 4.5–5 Ma, sedimentation was extremely slow or absent at this site (Tada et al. 2015c; Kamikuri et al. 2017).

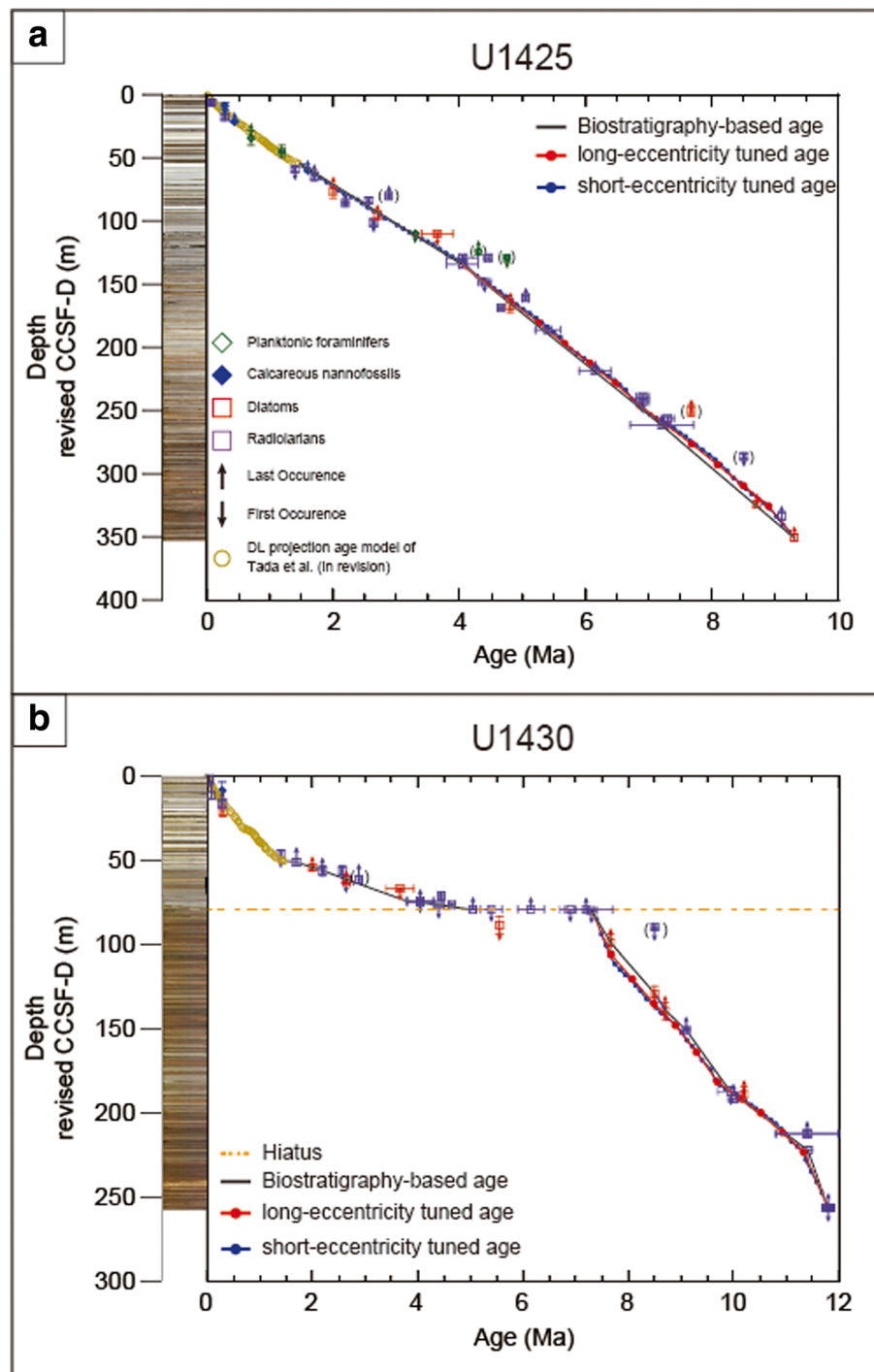


Fig. 2 Age-depth plot of sites U1425 and U1430. Biostratigraphic age control points are shown as symbols. Symbols with parentheses are biostratigraphic datums that are considered as less reliable. Detail explanation is given in the text. 405- and 100-kyr correlation points are also shown (red and blue circles). **a** U1425, **b** U1430

Method

Correlation with logging data

Continuous sedimentary records are required to apply cyclostratigraphy to sedimentary sequences. IODP expedition 346 drilled two or more holes at sites U1425

and U1430, from which a continuous Miocene–Pliocene stratigraphic record, or splice, was assembled for each site. During the expedition, the cores at each site were stratigraphically correlated onboard using physical properties such as natural gamma radiation (NGR), gamma

ray attenuation (GRA), and color reflectance (Tada et al. 2015b, 2015c). On the shore, core photographs were examined to identify small faults and disturbances that could not have been identified in the physical property profiles. The initial splice was revised on the basis of several new tie points within core intervals corresponding to lithological units I and III to correct miscorrelations and avoid intervals containing sponge plugs and other discontinuities (detailed in Irino et al. 2018). This study adopted the revised splices, in which the updated core composite depth below sea floor (CCSF-D) is referred to as the revised CCSF-D in this paper, and all core depths referred to hereafter are revised CCSF-D depths. The revised CCSF-D for site U1425 is CCSF-D patched rev20170309 in Irino et al. (2018), and the revised CCSF-D for site U1430 is CCSF-D patched rev20160113 in Irino et al. (2018). To check the validity of these revised splices, we correlated the revised composite NGR data with the hostile standard gamma ray (HSGR) logging data from sites U1425 and U1430. Downhole logs are unaffected by core expansion because they were acquired in situ, and their records are perfectly continuous with depth. For this reason, core-log integration helps in identifying miscorrelations that may be present (e.g., deMenocal et al. 1992; Lofi et al. 2016).

In our comparison of the revised NGR splices and the downhole HSGR logs (acquired in hole B at each site), we found strong correlations at the meter scale (Fig. 3). This confirms the validity of the revised splice as there were no significant core gaps deeper than ~80 m at sites U1425 and U1430. Correlation points between NGR and HSGR at sites U1425 and U1430 are listed in Tables 1 and 2. Correlation points occur every ~5 m in the record from both sites. This resolution ensured that no orbital eccentricity cycles were missing.

It should be noted that gamma ray attenuation by the steel hole casing precluded such a comparison in the upper ~80 m at both sites. However, three holes were drilled in this depth range at both sites, such that the revised splices were considered reliable despite the lack of core-log integration.

Chronology

To produce an orbitally tuned age model, we used the shipboard biostratigraphic data described in Tada et al. (2015b, 2015c) for sites U1425 and U1430 and additional radiolarian datums from Kamikuri et al. (2017).

The biostratigraphic age model for site U1425 extended from 9.3 Ma, the oldest age constraint within the

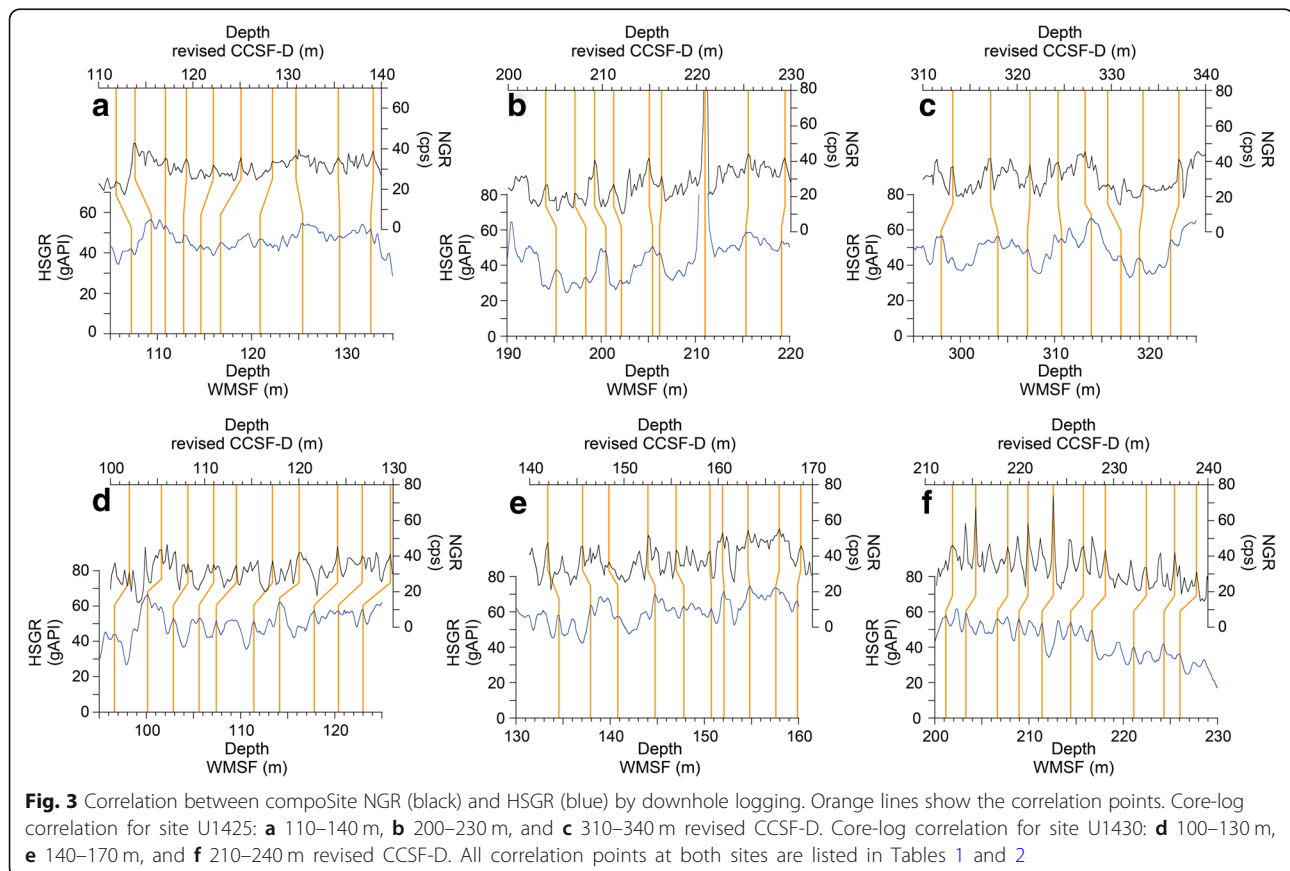


Table 1 Correlation points between revised composite core depth below seafloor (revised CCSF-D) and wireline log matched depth below sea floor (WMSF) at site U1425

Site U1425							
Hole	Core	Type	Sect	Depth from top of the section (cm)	Depth CSF-A (m)	Depth revised CCSF-D (m)	Depth WMSF (m)
D	12	H	3	30	102.6	108.285	103.024
D	13	H	2	70	106.2	111.849	107.2352
B	14	H	2	110	108.6	113.872	109.3408
B	14	H	4	130	111.83	117.102	110.8448
B	14	H	6	50	114.03	119.302	112.8
D	14	H	2	90	116.1	122.168	114.6048
B	17	H	2	150	120.8	125.111	116.7104
D	15	H	4	30	123.2	128.43	120.9216
D	15	H	5	130	125.7	130.930	125.4336
D	16	H	1	110	129	135.421	129.344
D	16	H	4	30	132.72	139.141	132.6528
D	16	H	6	90	136.32	142.741	135.9616
B	21	H	4	30	141.4	146.968	140.9248
B	21	H	6	50	144.6	150.168	144.384
D	18	H	5	70	146.1	152.474	146.1888
B	22	H	3	50	149.6	156.228	149.1968
B	22	H	5	70	152.8	159.428	152.656
D	19	H	4	130	154.7	162.399	154.912
B	23	H	3	90	159.5	166.468	158.672
B	23	H	6	50	163.6	170.568	162.1312
D	20	H	5	110	165.5	173.492	164.8384
B	24	H	3	90	169	176.800	169.0496
D	21	H	3	50	171.4	179.491	171.1552
D	21	H	6	10	175.5	183.591	175.5168
B	25	H	4	90	180	187.840	179.1264
D	22	H	4	130	183.2	192.039	183.1872
B	26	H	2	110	186.7	196.105	187.0976
D	23	H	3	50	190.4	199.085	190.4064
D	23	H	6	90	195.3	203.985	195.2192
B	27	H	4	50	198.6	207.082	198.3776
B	27	H	5	110	200.7	209.182	200.4832
D	24	H	4	90	201.8	211.196	202.1376
B	28	H	2	110	205.7	214.978	205.4464
B	28	H	3	90	207	216.278	206.1984
D	25	H	4	50	210.6	220.883	211.0112
B	29	H	3	130	215.9	225.473	215.3728
B	29	H	6	70	219.8	229.373	219.1328
B	30	H	3	30	224.4	234.212	223.7952
B	30	H	5	30	227.4	237.212	226.9536
D	28	H	5	30	230.9	240.128	229.5104
B	32	H	2	70	232.8	243.086	231.1648
D	29	H	2	110	236.7	246.37	235.5264

Table 1 Correlation points between revised composite core depth below seafloor (revised CCSF-D) and wireline log matched depth below sea floor (WMSF) at site U1425 (*Continued*)

Site U1425							
Hole	Core	Type	Sect	Depth from top of the section (cm)	Depth CSF-A (m)	Depth revised CCSF-D (m)	Depth WMSF (m)
B	33	H	3	130	238.6	249.122	237.7824
B	33	H	5	90	241.2	251.722	240.4896
D	30	H	5	50	245.3	255.969	245.7536
B	34	H	4	30	248.6	259.059	248.4608
B	34	H	5	110	250.9	261.359	250.8672
D	31	H	4	10	252.9	264.151	253.5744
B	35	H	3	70	257	267.448	256.5824
B	35	H	5	110	260.4	270.848	259.2896
D	32	H	3	130	262.1	273.966	262.2976
D	32	H	6	70	266	277.866	266.0576
B	37	H	2	110	270.1	281.540	269.968
B	38	H	1	70	272.9	283.901	272.8256
D	35	H	2	110	276.7	288.839	277.0368
B	39	H	4	30	281.33	292.896	280.0448
D	37	H	1	50	284	297.418	284.7072
D	37	H	4	150	288.49	301.908	288.016
D	37	H	7	50	291.17	304.588	290.1216
D	38	H	2	110	294.6	308.184	294.3328
D	39	H	2	90	299.1	313.181	297.9424
B	44	H	3	110	303.1	317.19	303.9584
D	40	H	3	110	305.5	321.36	307.1168
D	41	H	3	10	309.2	324.355	310.7264
B	47	H	1	130	314.4	327.223	313.8848
B	47	H	3	70	316.8	329.623	317.0432
D	43	H	3	30	318.8	333.363	318.9984
D	43	H	5	110	322.6	337.163	322.3072
B	49	H	3	30	325.8	340.342	325.3152

splice, to 1.45 Ma, the end of the orbitally tuned cyclostratigraphic age model for site U1425 (Tada et al. 2018). All biostratigraphic datums used are plotted in Fig. 2 and listed in Additional file 1. The following datums were discarded. The last occurrence (LO) and first occurrence (FO) of the planktonic foraminifer *Globorotalia ikebei* were determined by its rare occurrence in only one sample, and its presence was attributed to reworking (Tada et al. 2015b). The LO of the diatom *Thalassiosira schraderi* had a relatively large age uncertainty and was not used (Tada et al. 2015b). The LO of the radiolarian *Hexacontium parviakitaensis* in the Japan Sea was estimated as 2.87–2.90 Ma by Kamikuri et al. (2017), who placed this datum at 86.99 m, whereas the trend from our estimated sedimentation rates suggested that the LO of *H. parviakitaensis* should be at 81.01 m, and we could not rule out reworking. Finally,

the FO of the radiolarian *Cycladophora sphaeris* (= *Cycladophora sakaii* in Kamikuri et al. 2004, 2007) has age uncertainties of ~0.5 Myr between the eastern North Pacific, western North Pacific, and the Bering Sea (Kamikuri et al. 2004, 2007).

The biostratigraphic age model for site U1430 extended from 11.8 to 1.45 Ma (Fig. 2b). The LO of *Hexacontium parviakitaensis* was excluded for consistency with site U1425. The linear sedimentation rates (LSR) for the stratigraphic interval corresponding to 5 to ~1.45 Ma were too low (~1 cm/kyr) to detect meaningful orbital-scale changes in GRA, and the radiolarian datums and the occurrence of a glauconite layer suggest a hiatus during the time interval from 7 to 5 Ma (Kamikuri et al. 2017; Matsuzaki et al. 2018; Tada et al. 2015c). For this reason, we conducted an orbital tuning only for 11.8 to 7.3 Ma.

Table 2 Correlation points between revised composite core depth below seafloor (revised CCSF-D) and wireline log matched depth below sea floor (WMSF) at site U1430

Site U1430							
Hole	Core	Type	Sect	Depth from top of the section (cm)	Depth CSF-A (m)	Depth revised CCSF-D (m)	Depth WMSF (m)
A	11	H	4	10	93.7	98.93378	94.1832
B	11	H	3	30	97.1	102.0074	96.6216
B	11	H	5	70	100.5	105.4074	100.1268
A	12	H	3	70	102.3	108.2382	102.87
B	12	H	2	70	105.5	110.9596	105.6132
B	12	H	4	10	107.9	113.3596	107.442
A	13	H	2	90	110.5	117.2062	111.4044
B	13	H	1	110	113.9	120.0207	114.1476
B	13	H	4	70	118	124.1207	117.8052
B	13	H	6	30	120.6	126.7207	120.396
A	14	H	4	50	122.6	129.7123	122.9868
B	14	H	3	70	126	132.7575	125.73
B	14	H	6	30	130.1	136.8575	129.9972
A	15	H	4	70	132.3	139.8281	132.8928
B	15	H	2	130	134.6	141.9267	134.5692
B	15	H	5	50	138.3	145.6267	137.922
A	16	H	3	50	140.1	148.4069	140.8176
B	16	H	3	50	144.8	152.5529	144.78
B	16	H	5	50	147.8	155.5529	147.828
A	17	H	3	110	150.2	159.1428	150.7236
B	17	H	2	10	152.4	160.4806	152.0952
B	17	H	3	130	155.1	163.1806	154.8384
B	17	H	6	10	158.4	166.4806	157.5816
A	18	H	3	110	159.7	168.7812	159.8676
B	18	H	3	30	163.6	172.4537	163.2204
B	18	H	4	70	165.5	174.3537	164.7444
B	18	H	6	10	167.9	176.7537	167.3352
A	19	H	4	10	169.7	179.3117	169.6212
B	19	H	3	90	173.7	182.7136	173.8884
B	19	H	5	50	176.3	185.3136	176.022
A	20	H	2	110	177.2	187.4457	177.8508
B	20	H	1	70	180	189.7139	180.1368
B	20	H	3	110	183.4	193.1139	183.1848
B	20	H	5	50	185.8	195.5139	185.4708
A	21	H	4	10	188.1	199.0353	188.8236
B	21	H	2	50	190.8	202.5076	190.6524
B	21	H	4	10	193.4	205.1076	193.0908
A	22	H	3	150	197.5	209.5986	197.358
A	22	H	6	30	200.8	212.8986	201.168
B	22	H	4	90	203.7	215.3605	203.3016
B	22	H	6	130	207.1	218.7605	206.6544
A	23	H	5	30	208.5	220.9178	208.9404

Table 2 Correlation points between revised composite core depth below seafloor (revised CCSF-D) and wireline log matched depth below sea floor (WMSF) at site U1430 (*Continued*)

Site U1430							
Hole	Core	Type	Sect	Depth from top of the section (cm)	Depth CSF-A (m)	Depth revised CCSF-D (m)	Depth WMSF (m)
B	23	H	3	70	211.5	223.5968	211.3788
B	23	H	5	90	214.7	226.7968	214.4268
A	24	H	4	10	216.3	229.1107	216.7128
B	24	H	3	130	221.6	233.4764	221.1324
B	24	H	5	130	224.6	236.4764	224.3328
A	25	H	4	50	226.2	238.7943	226.0092
A	25	H	5	130	228.5	241.0943	228.6
B	25	H	4	110	232.4	244.2598	231.8004
A	26	H	2	50	232.7	246.2652	233.7816
B	26	H	3	70	238.3	250.4556	237.8964

Cyclostratigraphy

Quaternary sediments in the Japan Sea contain alternating dark- and light-colored layers that were synchronously deposited on the millennial scale, providing a tool for high-resolution correlation (Tada et al. 2018). An age model for the upper part of unit I (1.45–0 Ma) was established at site U1424 by Tada et al. (2018) by correlating the onboard GRA record of Tada et al. (2015b, 2015c) (regarded as a proxy of sea level) with the LR04 oxygen isotope ($\delta^{18}\text{O}$) sequence of Lisiecki and Raymo (2005), which allows ages of each of the dark layers at site U1424 to be extended to other sites. The orbitally tuned age model proposed here thus applies to the sedimentary sequence older than 1.45 Ma.

The Japan Sea sediments are composed of biosiliceous clay to silty clay (Tada et al. 2015b, 2015c). In biosiliceous sediments, GRA reflects the ratio of detritus to diatoms and decreases as diatom content increases because diatom frustules have high internal porosity (Tada and Iijima 1983). Diatom abundance is strongly linked to sea level because the surface productivity of the Japan Sea is controlled by the influx of nutrients through Tsushima Strait, which in turn has been modulated by glacio-eustatic sea-level changes (Tada et al. 2018). GRA likewise increases as the input of detritus increases. During sea-level lowstands, for instance, more terrigenous sediment should reach the study sites in the Japan Sea as the exposed area of the paleo-Japanese islands increases and the distance from the shoreline decreases, and the consequent increase in the mass accumulation rate of detritus (Tada 1991) results in higher GRA values. Thus, GRA can be used as a sea-level proxy.

To use GRA as a proxy, noise was first removed from the composite onboard GRA data (Tada et al. 2015b, 2015c). GRA values below the specific gravity of seawater (1.02 g cm^{-3}) were discarded, as were data corresponding to tephra and cracked intervals. The filtered

GRA profiles for sites U1425 and U1430 are presented in Additional file 2. We next performed a spectral analysis of the filtered GRA data to assess their fit to our tuned biostratigraphic age model using REDFIT software (Schulz and Mudelsee 2002). We generated Gaussian-filtered GRA time-series for both sites and assessed their correlation with temporal variations of Earth's orbital parameters, including long-eccentricity cycles (405 kyr) and short-eccentricity cycles (100 kyr) calculated by Laskar et al. (2004). For the Gaussian band-pass filtering, we used AnalySeries 2.0.8 software (Paillard et al. 1996) to sample evenly spaced data points from unevenly spaced original data. Band-pass filters were centered at 0.0025 kyr^{-1} (0.0005 kyr^{-1} bandwidth) and at 0.01 kyr^{-1} (0.003 kyr^{-1} bandwidth) to extract 405- and 100-kyr cycles, respectively. Tuning assumed no phase lag between GRA variability and orbital parameters, because the response time of an ice sheet is not known in this time interval (Holbourn et al. 2007).

To further improve our orbitally tuned age model, we tuned the GRA data from site U1425 to the oxygen isotope record, which is sensitive to sea-level fluctuation. The site U1425 record was chosen for its continuity and for its wide range of variability, which aided the tuning process. We tuned these data to the LR04 oxygen isotope record of Lisiecki and Raymo (2005) for 5.3–1.4 Ma and the benthic oxygen isotope record of Holbourn et al. (2018) from ODP site 1146 in the South China Sea for 10–5.2 Ma.

Results: orbital tuning

A critical part of orbital tuning is the choice of the initial tie point. For site U1425, we used the dark layer no. 21–2 projection tie points of Tada et al. (2018), which are at 1.45 Ma at 54.79-m-core depth. These have an error margin of about 4 kyr, inherited from the LR04 age model used as a tuning target. This error is negligible

for our purposes, and for site U1425, we assumed that the proposed depth-age model has no lag. It was more difficult to define the age model for site U1430 because of the presence of the hiatus. Following Kamikuri et al. (2017), we assumed that the hiatus ended at the FO of the radiolarian *Lychnocanoma parallelipes*, at 80.057 m (Irimo et al. 2018). The FO of *L. parallelipes* is 7.2–7.4 Ma (Kamikuri et al. 2017); therefore, we assumed that the FO of this species is at 7.3 ± 0.1 Ma. This implies that the proposed depth-age model for site U1430 has an error margin of 0.1 Myr.

The results of our spectral analysis show that the GRA data at both sites have a characteristic cyclicity that can be correlated with orbital cycles. At site U1425, peaks around 0.0025 and 0.01 that are significant above the 80% confidence level correspond to the long and short-eccentricity cycles, respectively, and peaks around 0.024 may be attributable to obliquity cycles (Fig. 4a). At site U1430, the power spectrum also shows a clear peak at 0.0025, a peak at 0.0057 that corresponds to the long obliquity cycle (174 kyr), and peaks around 0.024 that correspond to the 41-kyr obliquity cycle, although a short-eccentricity peak is absent (Fig. 4b). In sum, the GRA data displayed orbital signals at both sites, which we used to construct orbitally tuned age models.

We constructed an age model for each site in two steps. First, 405-kyr-filtered GRA profiles from our biostratigraphic age model were tuned to the long (405 kyr) eccentricity cycle. Because this cycle has a stable periodicity over the last 250 Myr, it is well suited for cyclostratigraphy (Hinnov 2000; Laskar et al. 2004; Hinnov and Hilgen 2012). Second, we tuned the resulting GRA profiles to the short-eccentricity cycle by correlating eccentricity minima with 100-kyr-filtered GRA maxima under the assumption that sea-level lowstands occur during eccentricity minima that increase the influx of detritus to the Japan Sea and thus raise GRA values, as explained previously.

The 405-kyr eccentricity cycle is relatively weak in benthic oxygen isotope records younger than about 5 Ma (Zachos et al. 2001; de Boer et al. 2014), although both 405-kyr and 100-kyr eccentricity cycles are clear in benthic carbon and oxygen isotope records from the Oligocene and Miocene (Pälike et al. 2006; Liebrand et al. 2011, 2016, 2017; Holbourn et al. 2013a, 2013b; Beddow et al. 2016). Accordingly, we did not use the 405-kyr eccentricity cycle as a tuning target after 5.0 Ma at site U1425. The plot of 405-kyr-filtered GRA records based on the biostratigraphic age model and the long-eccentricity cycle from 9.3 to 5 Ma at site U1425 shows that the two records are nearly a half-wavelength out of phase (Fig. 5a). We tuned the GRA maxima to the nearest eccentricity minima to yield the result shown in Fig. 5b. There are 10 correlated cycles in this time

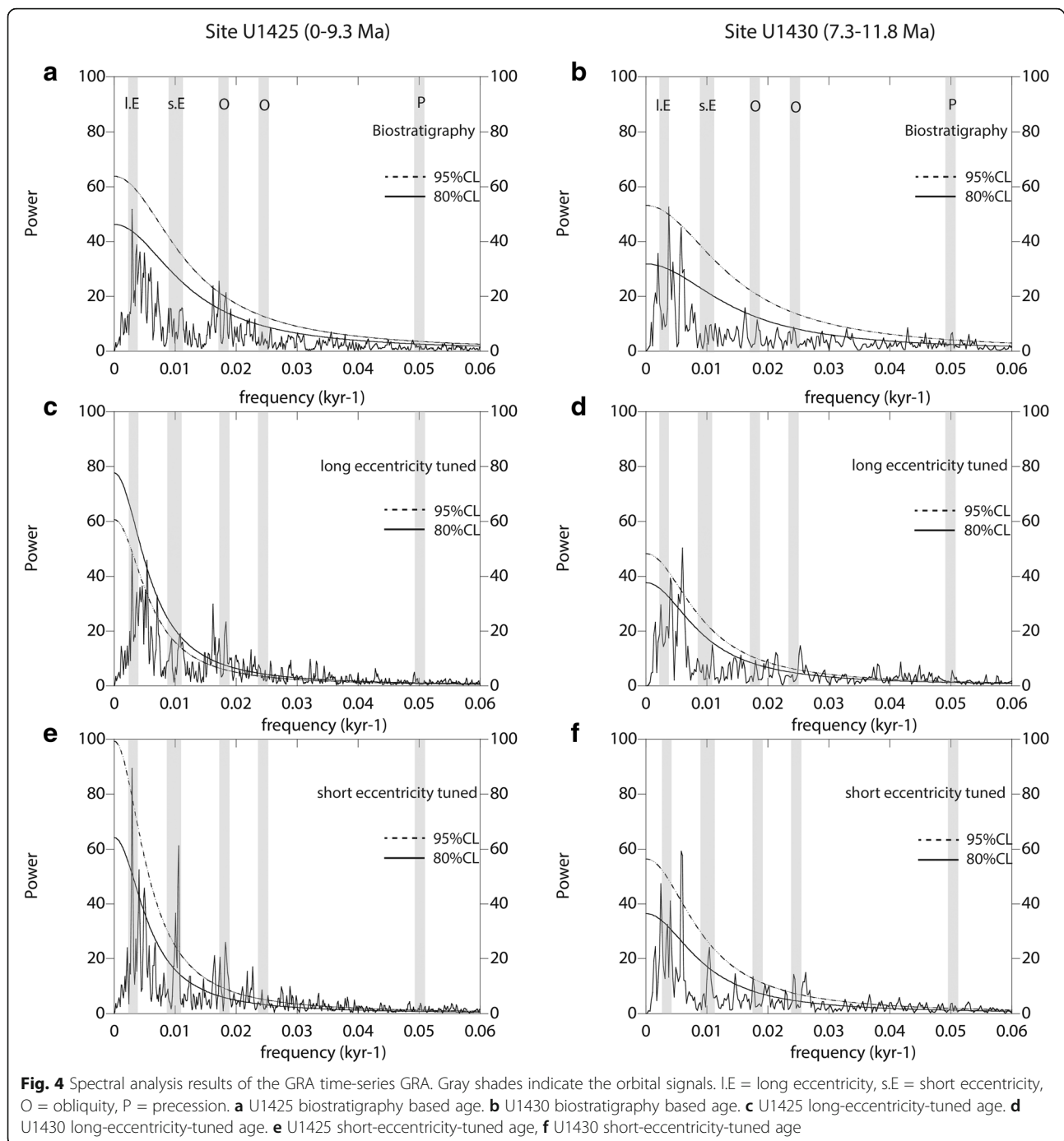
interval. The mismatch in amplitudes between the GRA signals and eccentricity from 6.2 to 7.5 Ma (Fig. 5b) means that amplitude modulation of GRA by the long-eccentricity cycle is not established for the 9.3–5 Ma interval.

Using an age model based on the long-eccentricity-tuned age model for 9.3–5 Ma and the biostratigraphic model for 5–1.45 Ma, we conducted short-eccentricity tuning to correlate the GRA record and the short-eccentricity (100 kyr) cycle. Both GRA and eccentricity were filtered with a 100-kyr filter using Gaussian band-pass filtering (see the “Method” section), and GRA maxima were correlated with eccentricity minima (Fig. 6a and b). The amplitudes of the two records were well matched except from 6.6 to 3.6 Ma, when the overall amplitude of GRA was small regardless of eccentricity (Fig. 6b). The depths and ages of the 405- and 100-kyr correlation points for site U1425 are listed in Tables 3 and 4 and plotted in Fig. 2a, which shows that orbitally tuned correlation points are consistent with the biological datums.

We applied the same procedure to build an orbitally tuned age model for the 11.8–7.3 Ma interval at site U1430, first correlating the 405-kyr-filtered GRA maxima with long-eccentricity minima (Fig. 5c and d), then refining the age model by correlating peaks in the 100-kyr-filtered GRA and short-eccentricity records (Fig. 6c and d). The 405-kyr and 100-kyr correlation points are listed in Tables 3 and 4 and plotted against depth in Fig. 2b.

We checked the validity of the tuned results by comparing their power spectra to the power spectra of the biostratigraphic age models (Fig. 4a and f). At site U1425, GRA peaks after short-eccentricity tuning became stronger at 405, 100, and 41 kyr and exceeded the 95% confidence level, although other peaks were little changed (Fig. 4c and e). At site U1430, cycles of long eccentricity and obliquity were stronger after orbital tuning (Fig. 4b and d). Thus, we are confident that our two-step orbital tuning improved the accuracy of the age models at both sites because the orbital signals of the GRA power spectra were stronger across all orbital peaks (Fig. 4). In addition, we tuned the GRA record to the oxygen isotope record at site U1425 to check the validity of our assumption that GRA is sensitive to sea-level changes and to check the validity of the orbital tuning results. The results, given in Additional files 3, 4, 5, 6, 7, 8, 9, 10, 11, 12, and 13, indicate that our orbitally tuned age model is consistent with the $\delta^{18}\text{O}$ -tuned age model with a lag no greater than 40 kyr, or less than half of an eccentricity cycle.

Although the GRA power spectra before orbital tuning had peaks attributable to obliquity and precession, we did not conduct tuning with respect to obliquity or precession because the obliquity and precession cycles have



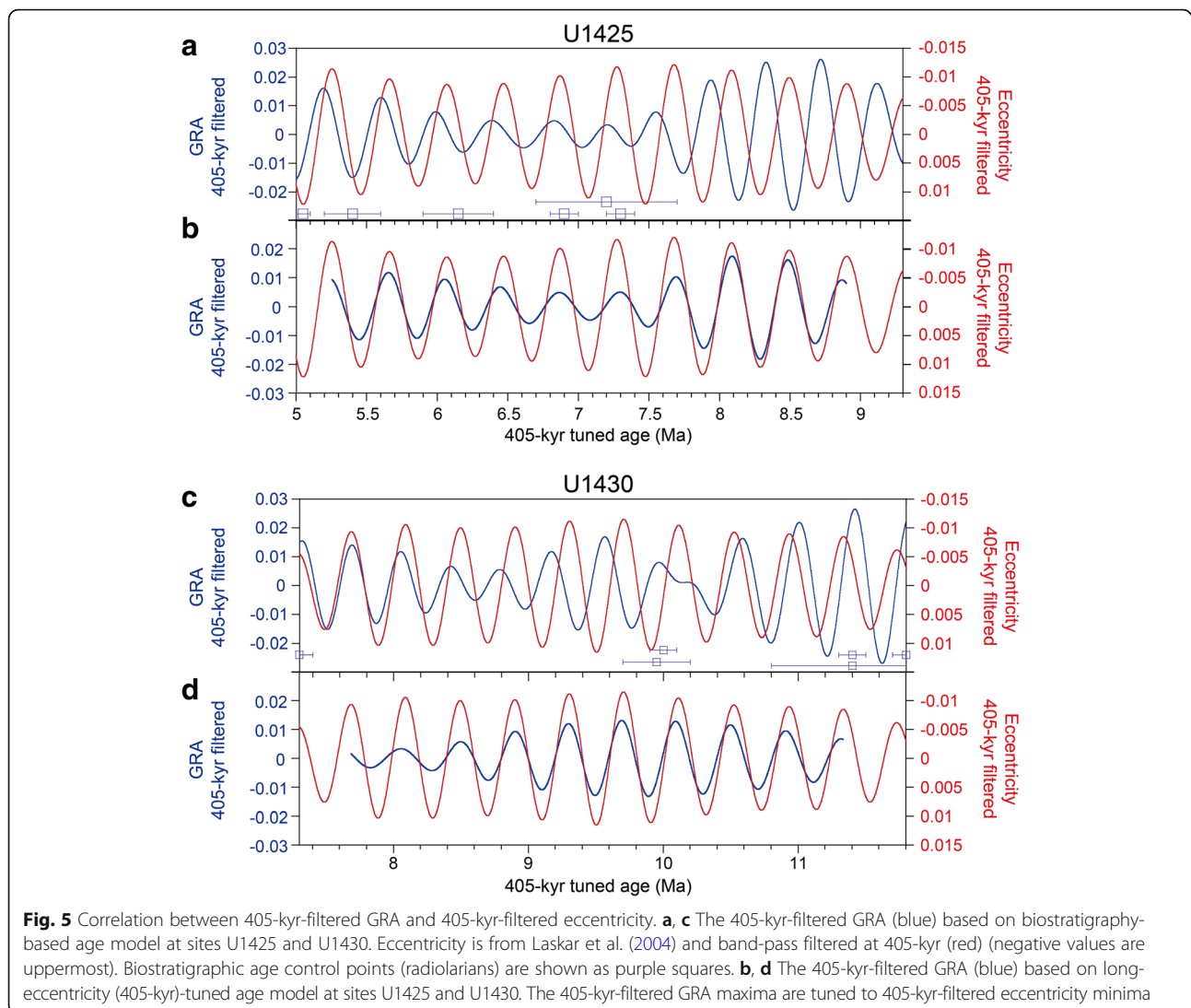
relatively high uncertainties owing to effects of tidal dissipation and changes in dynamical ellipticity, and because GRA amplitudes were too small during some time intervals.

Discussion

Comparison of physical properties with sea-level change

After adjusting our GRA records on the basis of our short-eccentricity-tuned age model, we compared them

to a previously published sea-level record. Miller et al. (2005) compiled two high-resolution benthic oxygen isotope records covering the last 9 Myr from ODP site 846 in the equatorial Pacific (Shackleton et al. 1995) and ODP site 982 in the northern North Atlantic (Hodell et al. 2001) and converted them to a record of eustatic sea level, using a calibration ratio of 0.1‰/10 m. In this record, sea-level fluctuations over glacial-interglacial cycles were roughly 40 m before ~ 6 Ma, gradually increased to



about 100 m by 1.5 Ma, then remained at that amplitude until the present (Miller et al. 2005).

For this comparison, we compiled the GRA dataset from both sites, then resampled it and the sea-level record of Miller et al. (2005) at 100-kyr intervals between 9 and 1.45 Ma. The result (Fig. 7) shows a fair correlation ($r = 0.63$) between the two datasets for this period. Between 6.6 and 3.6 Ma, the GRA amplitudes were small and the estimated sea levels were mostly restricted between 10 and -20 m. These lower values of estimated sea-level changes may be reflected in the low amplitude of the GRA dataset, and the correlation between GRA and estimated sea-level amplitude was slightly stronger when we excluded the data from 6.6 to 3.6 Ma ($r = 0.65$).

DeVleeschouwer et al. (2017) compiled a high-resolution benthic oxygen isotope record for the entire Neogene and Quaternary from multiple drill sites in the Atlantic, eastern equatorial Pacific, and South China Sea. We used this

record to compare the variabilities of NGR and GRA at sites U1425 and U1430 with the oxygen isotope record of benthic foraminifers since 12 Ma. The GRA and NGR data were well correlated with the benthic oxygen isotope record before 8 Ma and after 3.3 Ma (Fig. 8), including the last 1.45 Ma (Tada et al. 2018); however, the correlation was unclear between 8 and 3.3 Ma, when both datasets had orbital-scale variations of small amplitude.

In the benthic oxygen isotope record of Miller et al. (1991), excursions Mi-5 to Mi-7 occurred during the time interval covered by the Japan Sea sediments examined in this study. In their orbitally tuned age model based on Fe signals in South Atlantic shallow marine sediments, Westerhold et al. (2005) recognized the Mi-5 and Mi-6 events at 11.7 and 10.7–10.4 Ma, respectively. At site U1430, we recognized GRA and NGR maxima corresponding to these two events at 11.7 and 10.6 Ma, respectively (Fig. 8). The Mi-6 event is also clearly

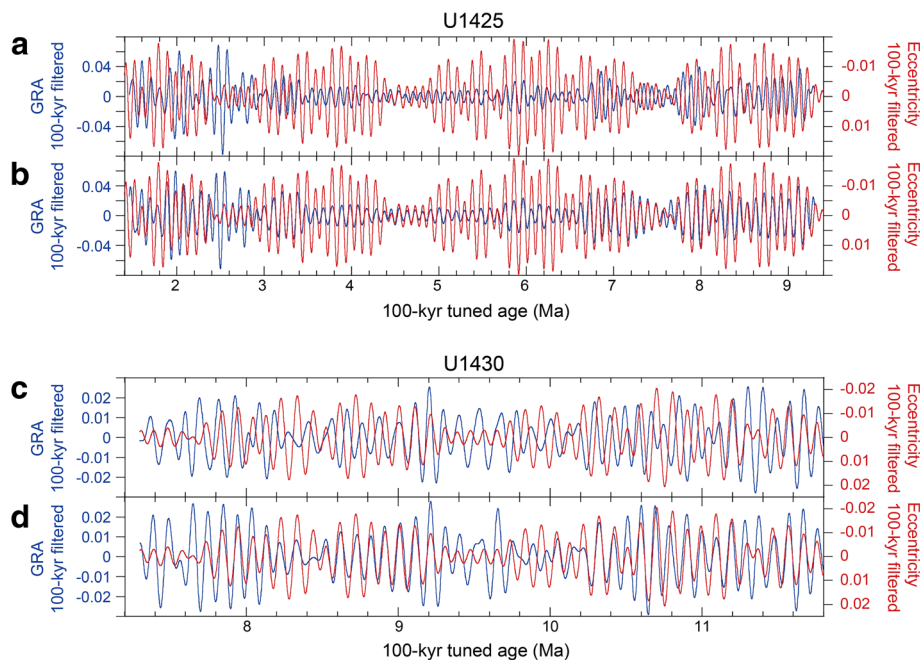


Fig. 6 Correlation between 100-kyr-filtered GRA and 100-kyr-filtered eccentricity. **a, c** The 100-kyr-filtered GRA (blue) based on long-eccentricity-tuned age model at sites U1425 and U1430. Eccentricity is filtered at 100-kyr (red). **b, d** The 100-kyr-filtered GRA (blue) based on short-eccentricity (100-kyr)-tuned age model at sites U1425 and U1430. The 100-kyr-filtered GRA maxima are tuned to 100-kyr-filtered eccentricity minima

evident as a cooling step in the benthic oxygen isotope record from ODP site 1146 in the South China Sea (Holbourn et al. 2013a). Although the age of the Mi-7 event is uncertain because the oxygen isotope signal has many small maxima between 9.6 and 9.0 Ma (Andersson and Jansen 2003; Westerhold et al. 2005), GRA and NGR maxima in the Japan Sea sediments are compatible with two candidate ages proposed by Westerhold et al. (2005), 9.4 and 8.7 Ma (Fig. 8). The close correspondence between physical properties and sea-level changes such as the Mi events tends to confirm the accuracy of short-eccentricity-tuned age models. In addition, our

results support the possibility that the amplitude of sea-level changes can be estimated from GRA data independent of oxygen isotope values.

Correlation between sites U1425 and U1430

Figure 8 shows the temporal variations of NGR, GRA, and LSR for the last 12 Myr at sites U1425 and U1430. The sedimentary record at site U1425 extends back to 9.3 Ma without any stratigraphic gaps, whereas the sedimentary record at site U1430 from 11.8 to 0 Ma is interrupted by a probable hiatus from ~7.3 to 4.5–5 Ma. Thus, comparisons of the two records are limited to the

Table 3 405-kyr correlation points for sites U1425 and U1430

Site U1425		Site U1430	
405-kyr tie point			
Depth revised CCSF-D (m)	Age (Ma)	Depth revised CCSF-D (m)	Age (Ma)
180.44	5.253	106.149	7.685
196.92	5.661	120.443	8.087
212.60	6.067	134.881	8.494
228.62	6.469	147.914	8.899
246.48	6.869	163.999	9.303
261.72	7.272	181.452	9.705
276.29	7.677	191.255	10.112
292.75	8.085	200.029	10.524
309.34	8.493	211.634	10.934
325.72	8.901	223.129	11.337

Table 4 100-kyr correlation points for sites U1425 and U1430

Site U1425		Site U1430	
100-kyr tie point			
Depth revised CCSF-D (m)	Age (Ma)	Depth revised CCSF-D (m)	Age (Ma)
55.946	1.516	84.790	7.391
59.207	1.601	93.418	7.483
62.382	1.686	100.319	7.578
65.415	1.789	106.378	7.649
69.048	1.892	110.904	7.737
72.280	1.985	114.716	7.842
75.513	2.071	117.860	7.948
78.202	2.170	120.433	8.045
80.462	2.276	123.903	8.131
83.180	2.381	127.088	8.229
85.983	2.456	131.889	8.336
89.044	2.542	137.126	8.526
91.933	2.639	140.317	8.617
94.565	2.730	143.508	8.722
97.712	2.816	147.174	8.914
102.718	3.001	152.226	9.008
106.037	3.106	156.441	9.110
108.869	3.206	160.069	9.214
111.472	3.293	163.750	9.309
114.104	3.387	168.265	9.389
116.478	3.490	174.024	9.566
118.824	3.588	180.365	9.651
121.856	3.677	183.205	9.737
125.318	3.777	185.497	9.837
128.579	3.883	188.660	10.043
131.297	3.984	191.300	10.129
133.986	4.075	192.841	10.219
143.123	4.273	195.096	10.322
146.313	4.377	197.265	10.424
149.360	4.455	199.348	10.510
153.016	4.540	201.551	10.596
155.883	4.636	204.016	10.701
159.360	4.728	206.292	10.806
162.550	4.815	209.250	10.903
166.027	4.900	212.137	10.992
169.611	5.000	216.724	11.092
173.052	5.106	219.361	11.197
176.314	5.207	222.113	11.298
179.862	5.292	227.669	11.368
183.565	5.381	234.373	11.465
187.524	5.484	240.310	11.569
191.861	5.585	247.013	11.669

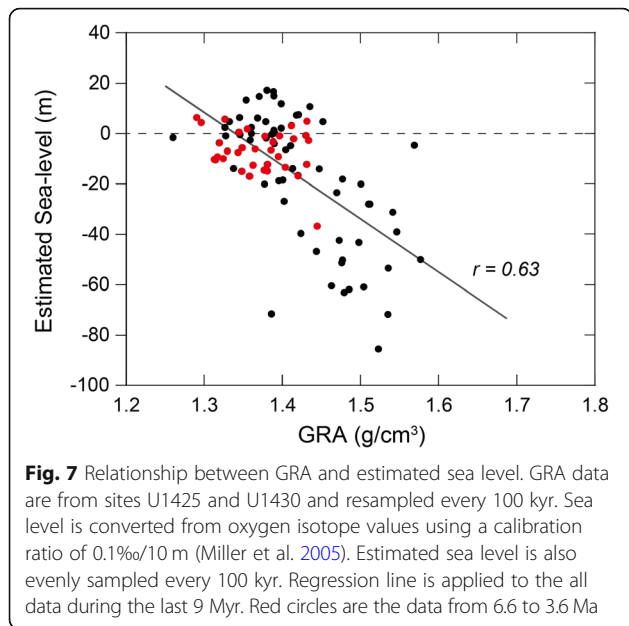
Table 4 100-kyr correlation points for sites U1425 and U1430 (Continued)

Site U1425		Site U1430	
100-kyr tie point			
Depth revised CCSF-D (m)	Age (Ma)	Depth revised CCSF-D (m)	Age (Ma)
197.275	5.666	253.812	11.756
201.098	5.754		
204.850	5.859		
208.746	5.963		
212.064	6.059		
215.100	6.151		
219.194	6.252		
222.841	6.355		
226.079	6.450		
229.736	6.532		
233.783	6.628		
241.000	6.728		
245.840	6.821		
249.576	6.910		
252.965	7.008		
256.108	7.113		
258.615	7.213		
261.334	7.302		
264.343	7.389		
267.569	7.483		
270.559	7.578		
274.020	7.649		
277.249	7.737		
280.943	7.842		
284.636	7.948		
288.443	8.045		
292.552	8.131		
297.181	8.229		
303.141	8.336		
307.393	8.441		
311.580	8.526		
315.856	8.617		
319.532	8.722		
323.321	8.823		
327.455	8.914		
333.349	9.008		
339.879	9.110		
345.889	9.214		

periods 9.3–7.3 and 5–1.5 Ma (Fig. 8). We therefore compiled NGR, GRA, and LSR time-series using the age model of Tada et al. (2018) for the uppermost part of both sites, biostratigraphic data for the 5.0–1.5 Ma

interval at site U1430, and our short-eccentricity-tuned age models (Fig. 2).

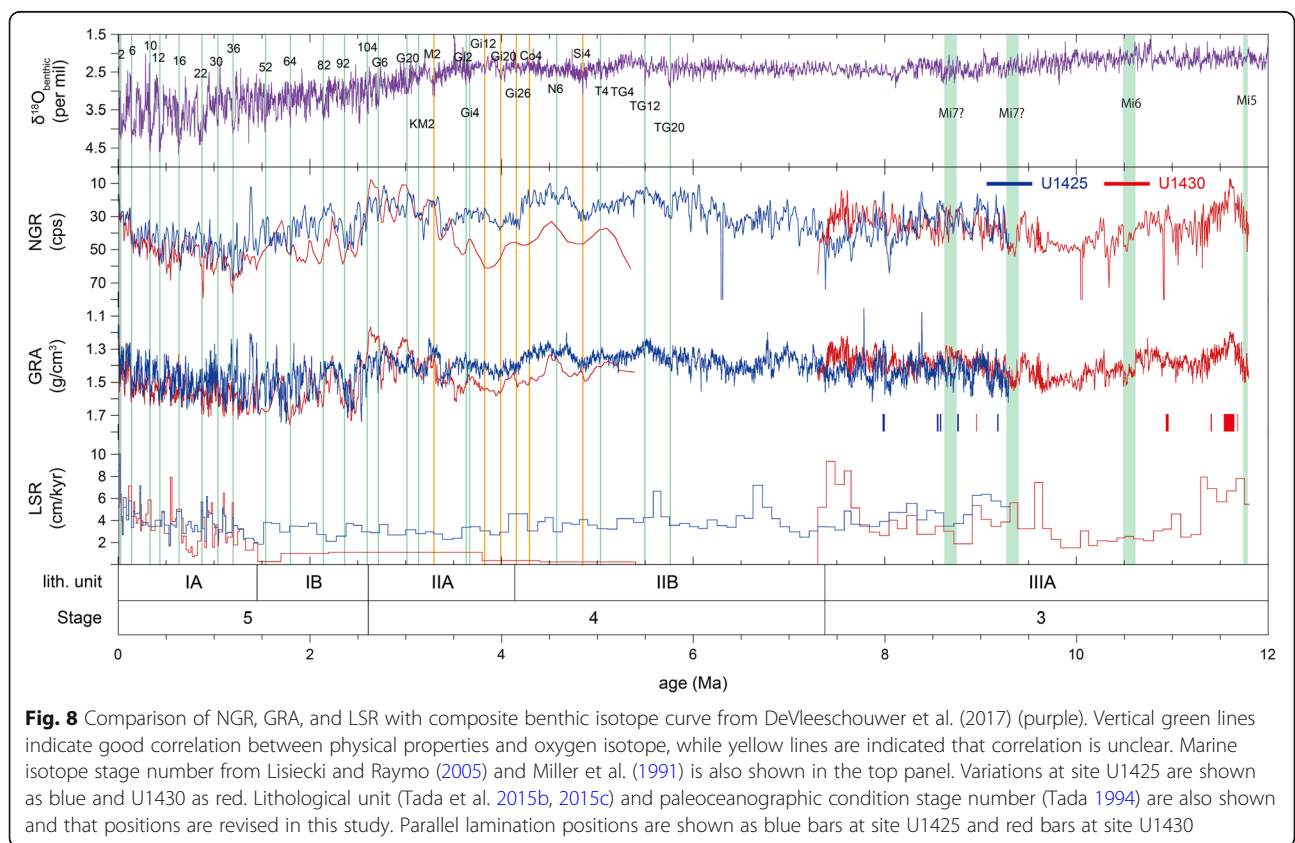
In general, temporal changes in GRA and NGR were well correlated between the two sites from 3.5



to 0 Ma. From 5.3 to 3.5 Ma, GRA and NGR values were higher at site U1430 than at site U1425 (Fig. 8), a difference that can be explained by the fact that the sediment at site U1430 is less diatomaceous or more tuffaceous than at U1425 (Tada et al. 2015b, 2015c). From 9.3 to 7.3 Ma,

GRA and NGR curves at the two sites were similar. The close correspondence in physical properties suggests that paleoceanographic conditions were similar at sites U1425 and U1430.

During the hiatus interval at site U1430 from 7.3 to 5.3 Ma, there were no significant changes in physical properties and LSR at site U1425 (Fig. 8) or in LSRs at ODP sites 794, 795, and 797 also located in the Japan Sea (Tada 1994). The Late Miocene hiatuses have been reported from some on-land sections in northeastern Japan (Watanabe 1994), but these correspond to the diatom datums 5D, 6A, and 6B (Akiba 1986; Yanagisawa and Akiba 1998; Tada et al. 2015a, 2015c), which range in age from 9.3 to 7.6 Ma. The hiatus at site U1430 coincides in depth with a major regional unconformity on seismic profiles (MB3 unconformity in Horozal et al. 2017) that extends over much of the eastern South Korea plateau where site U1430 was drilled. The origin of this unconformity is unclear. Watanabe (1994) and Horozal et al. (2017) attributed it to erosion by bottom currents or a brief episode of tectonic uplift. Whatever its origin, this hiatus must reflect a local, basin-scale event because there are no drastic changes in LSRs in this time interval in other Japan Sea cores.



Revision of lithological divisions at sites U1425 and U1430

Tada et al. (2015b, 2015c) defined a set of lithological units in Japan Sea sediments, of which the latest four (I to IV) and their subunits are represented in the sediments treated in this study. The revised GRA, NGR, and logging profiles and the revised age model constructed in this study lead us to propose revisions of the boundaries of these units and subunits.

Tada et al. (2015b, 2015c) stated that unit I is characterized by decimeter-scale intervals of alternating light and dark sediment and that the boundary between subunit IA and the underlying subunit IB is distinguished by a downward decrease in the frequency of these alternations. They placed the base of subunit IB at 50.7 m at site U1425 and at 46.9 m at Site U1430; however, this change in frequency occurs deeper, at 54.8 m at site U1425 and 50.7 m at site U1430, as shown by lithological observations as well as NGR and GRA data (Fig. 8). The same discrepancy is also observed at other IODP expedition 346 sites in the Japan Sea (Tada et al. 2018; Irino et al. 2018). The age of the sediment at these revised boundary positions is 1.45 Ma (Tada et al. 2018). The NGR and GRA profiles in subunit IA (Fig. 8) display large, suborbital-scale fluctuations after 1.45 Ma that correspond to the color banding in the sediments. The base of subunit IB is defined by a downward change in sediment color and increase in diatom content (Tada et al. 2015b, 2015c). The increase in diatom content corresponds to a clear decrease in NGR at 90.71 m at site U1425, ~1.5 m shallower than the depth specified by Tada et al. (2015b, 2015c), and 61.14 m at site U1430, the same depth specified in the original definition. The age of this boundary is 2.61 Ma according to our revised age model (Fig. 8). During deposition of unit IB, NGR and GRA fluctuated strongly, as they did in unit IA, but at a lower frequency than in unit IA.

In unit II, the boundary between subunits IIA and IIB is defined by a downward increase in diatom content, which is recorded as a downward decrease in NGR or GRA at 137.34 m at site U1425 (4.14 Ma in our age model) and 74.42 m at site U1430 (4.04 Ma in our age model). NGR data do not show a clear downward decrease at 74.42 m at site U1430, but this probably reflects the proximity of an NGR peak from a glauconite layer (e.g., Tada et al. 2015c) at ~78.8–79.7 m. The age of the boundary differs slightly between the two sites; however, the age of the upper hiatus at site U1430 is based on a biodatum, which has an error of about ± 0.1 Myr. Accordingly, the boundary positions are consistent between the sites.

Tada et al. (2015b, 2015c) distinguished unit III from unit II by its lower diatom content and darker sediment color, which is reflected in higher values of NGR and

GRA (Fig. 8). The boundary between units II and III (specifically, subunit IIB and subunit IIIA) is at 263.25 m at site U1425 and 84.81 m at site U1430, and its age is 7.36–7.39 Ma according to our age model (Fig. 8). Subunit IIIA is characterized by higher NGR and GRA values, with fluctuations of greater amplitude, than unit II reflecting the increased contrast between alternating light and dark layers.

In summary, our analysis shows that the revised lower boundaries of the lithological units of Tada et al. (2015b, 2015c) correspond to the following ages: 1.45 Ma for subunit IA, 2.61 Ma for subunit IB, 4.04–4.14 Ma for subunit IIA, and 7.36–7.39 Ma for subunit IIB.

Lithostratigraphic correlation of Japan Sea sites and refinement of paleoceanographic stages

The criteria for defining lithological units were basically the same for ODP leg 127/128 and IODP expedition 346. According to Tada and Iijima (1992), unit 1 in ODP leg 127/128 sediments is characterized by decimeter- to meter-scale alternations of dark and light silty clay to clay and is divided into subunits 1A and 1B on the basis of the frequency of dark layers and the intensity of bioturbation. Unit 2 is composed of clayey diatom ooze and diatomaceous clay that is heavily bioturbated and mottled, with alternating dark and light layers and a general darkening of sediments near its base. This unit is not subdivided. Unit 3 is characterized by decimeter- to meter-scale alternating light and dark layers, the latter being faintly laminated, and by a relatively high organic carbon content.

Tada (1994) compiled the paleoceanographic data of ODP leg 127/128 and paleogeographic data on the Japanese islands by Iijima and Tada (1990) to reconstruct the paleoceanographic evolution of the Japan Sea. The proposed stages of this history correspond to the lithological units of Tada and Iijima (1992). Given that correspondence, paleoceanographic stages 5, 4, and 3 of Tada (1994) are shown in Fig. 8 as coeval with lithological units I, II, and III, respectively.

At sites U1425 and U1430, the boundary between units III and II is based on the increase in diatom content and decrease in terrigenous content and is assigned an age of ~7.4 Ma. Tada (1994) described a dramatic increase in biogenic silica content around 8 Ma at the ODP leg 127/128 sites, which is probably correlated with this boundary. According to Tada (1994), during paleoceanographic stage 3, bottom water conditions fluctuated between anoxic and suboxic in association with eustatic sea-level changes. This history is consistent with the sporadic occurrence of parallel laminations in lithological subunit IIIA at sites U1425 and U1430, which suggests the suppression of bioturbation due to low oxygen levels (Fig. 8). The difference in the ages of parallel

laminations between the two sites may reflect the position of euxinic or anoxic water masses. The presence of parallel laminations only at site U1425 in the upper part of unit IIIA signifies euxinic or anoxic conditions in the bottom water there and oxic or suboxic conditions at site U1430, whereas the presence of parallel laminations only at site U1430 in the lower part of unit IIIA (~9.0 Ma) may indicate the development of an oxygen minimum zone within the Japan Sea, because site U1430 was at the appropriate paleo-water depth. Another line of evidence that an oxygen minimum zone developed or expanded in the Japan Sea around 8 Ma is radiolarian data indicating the presence of North Pacific type deep-water species at that paleo-water depth (Matsuzaki et al. 2018).

Paleoceanographic stage 4 (7.4–2.61 Ma) corresponds to lithological unit II, which is characterized by relatively low values of GRA and NGR at Site U1425. Tada (1994) suggested that during this stage, terrigenous input was diluted by diatoms due to higher productivity caused by enhanced production of deep water and consequent upwelling.

During paleoceanographic stage 5 (2.61–0 Ma), NGR and GRA fluctuated strongly at millennial to orbital scales, interpreted as the result of millennial-scale changes in the East Asian summer monsoon superimposed on glacio-eustatic sea-level changes (Tada et al. 2018). The deposition of lithological unit I is thought to have been initiated by a drop in sea level caused by the onset of northern hemisphere glaciation (Lisiecki and Raymo 2005; Tada et al. 2018).

Conclusions

Long-term composite sedimentary records from IODP sites U1425 and U1430 in the Japan Sea were interpreted using cyclostratigraphy to establish high-resolution age models for the time interval between 11.8 and 1.45 Ma. We used GRA to measure detrital cycles in the sediments, then tuned the GRA profiles to long (405 kyr) and short (100 kyr) eccentricity cycles. In the resulting orbitally tuned age model, NGR and GRA are strongly correlated with the estimated sea-level changes since 9 Ma. Although the changes in physical properties and benthic oxygen isotope ratios were relatively small before 3 Ma, they are shown here to coincide with large-scale sea-level changes such as Mi events. Using the short-eccentricity-tuned age model, we compared the physical properties and LSRs at sites U1425 and U1430 and found that the GRA and NGR profiles are strongly correlated where they overlap, suggesting that paleoceanographic conditions were similar at the two sites, the most notable difference being in paleoceanographic conditions during the deposition of subunit IIIA as signified by the occurrence of parallel laminations. By

correlating the lithological units at sites U1425 and U1430 with those at the sites drilled during ODP leg 127/128, we were able to refine the timing of changes in paleoceanographic conditions on the basis of our short-eccentricity-tuned age model. As a result, we revise the boundary ages of paleoceanographic stages proposed by Tada (1994), and their timings are consistent with other records.

Additional files

Additional file 1: All biostratigraphic datums used. (XLSX 234 kb)

Additional file 2: Filtered GRA profiles for sites U1425 and U1430. (XLSX 19 kb)

Additional file 3: GRA data tuned to LR04 oxygen isotopes records of Lisiecki and Raymo (2005) : 1.4-2.5 Ma. (JPG 2.54 mb)

Additional file 4: GRA data tuned to LR04 oxygen isotopes records of Lisiecki and Raymo (2005) : 2.4-3.5 Ma. (JPG 1.99 mb)

Additional file 5: GRA data tuned to LR04 oxygen isotopes records of Lisiecki and Raymo (2005) : 3.4-4.5 Ma. (JPG 1.97 mb)

Additional file 6: GRA data tuned to LR04 oxygen isotopes records of Lisiecki and Raymo (2005) : 4.4-5.5 Ma. (JPG 1.87 mb)

Additional file 7: GRA data tuned to oxygen isotopes records of Holbourn et al. (2018) : 5.4-6.5 Ma. (JPG 1.58 mb)

Additional file 8: GRA data tuned to oxygen isotopes records of Holbourn et al. (2018) : 6.4-7.5 Ma. (JPG 1.64 mb)

Additional file 9: GRA data tuned to oxygen isotopes records of Holbourn et al. (2018) : 7.4-8.5 Ma. (JPG 2.53 mb)

Additional file 10: GRA data tuned to oxygen isotopes records of Holbourn et al. (2018) : 8.4-9.3 Ma. (JPG 1.67 mb)

Additional file 11: Tie points obtained from oxygen isotopes tuning. (XLSX 38 kb)

Additional file 12: Comparison of orbital tuning results with oxygen isotopes tuning results. (JPG 851 kb)

Additional file 13: 1.45 to 9.3 Ma Oxygen isotope tuned GRA and NGR records. (JPG 2.32 kb)

Abbreviations

CCSF: Core composite depth below sea floor; FO: First occurrence; GRA: Gamma ray attenuation; HSGR: Hostile standard gamma ray; IODP: Integrated Ocean Drilling Program; LO: Last occurrence; LSR: Linear sedimentation rate; NGR: Natural gamma radiation; ODP: Ocean Drilling Program; TWC: Tsushima warm current; WMSF: Wireline log matched depth sea floor

Acknowledgements

We thank the technicians and scientists of IODP Expedition 346 for their efforts to acquire the shipboard data that were used in this work. We thank Dr. Martin Ziegler and Dr. Andrew C.G. Henderson, whose suggestions helped to greatly improve the manuscript. We also thank the Japanese shipboard scientists of Expedition 346 for constructive suggestions and comments.

Funding

This work was supported by a grant to the IODP Expedition 346 After Cruise Research Program, JAMSTEC, awarded to TR and IT, and by Japan Society for the Promotion of Science (JSPS) KAKENHI Grant Number 16H01765 awarded to TR. Work by MKM was partly financed by JSPS Research Fellowship for Young Scientist grant 16J02142.

Availability of data and materials

The filtered GRA data used in this study are available in Additional file 2.

Authors' contributions

All data were collected by expedition 346 scientists during the IODP expedition 346 cruise. KS conducted the orbital tuning of the GRA data and wrote a draft of the manuscript. TR proposed the topic and conceived and designed the study. MKM helped interpret the biostratigraphy, helped in revising the manuscript, and conducted the oxygen isotope tuning of the GRA data provided in the supplementary files. TI and LJ helped in the correlation of core and logging data. SK drew the figures and wrote a draft of the manuscript. All authors read and approved the final manuscript.

Authors' information

KS is a student of TR. TR was co-chief scientist of IODP Expedition 346. IT and LJ were shipboard scientists of IODP Expedition 346. MKM was a JSPS Postdoctoral researcher under TR, now assistant professor at the University of Tokyo.

Competing interests

The authors declare that they have no competing interests.

Publisher's Note

Springer Nature remains neutral with regard to jurisdictional claims in published maps and institutional affiliations.

Author details

¹Department of Earth and Planetary Science, Graduate School of Science, The University of Tokyo, 7-3-1 Hongo, Bunkyo-ku, Tokyo 113-0033, Japan. ²Present Address Atmosphere and Ocean Research Institute, The University of Tokyo, 5-1-5 Kashiwanoha, Kashiwa, Chiba 277-8564, Japan. ³Graduate School of Environmental Earth Science, Hokkaido University, Sapporo 060-0810, Japan. ⁴Géosciences Montpellier, Université Montpellier II, Place Eugène Bataillon, 34095 Montpellier Cedex 5, France.

Received: 28 September 2017 Accepted: 12 December 2018

Published online: 15 January 2019

References

- Akiba F (1986) Middle Miocene to Quaternary diatom biostratigraphy in the Nankai Trough and Japan Trench, and modified lower Miocene through Quaternary diatom zones for middle-to-high latitudes of the North Pacific. *Init Rep DSDP* 87:393–481.
- Andersson C, Jansen E (2003) A Miocene (8–12 Ma) intermediate water benthic stable isotope record from the northeastern Atlantic, ODP Site 982. *Paleoceanography* 18:1013. <https://doi.org/10.1029/2001PA000657>.
- Beddow HM, Liebrand D, Sliujs A, Wade BS, Lourens LJ (2016) Global change across the Oligocene-Miocene transition: high-resolution stable isotope records from IODP site U1334 (equatorial Pacific Ocean). *Paleoceanography* 31:81–97. <https://doi.org/10.1002/2015PA002820>.
- Bell DB, Jung SJA, Kroon D, Hodell DA, Lourens LJ, Raymo ME (2015) Atlantic deep-water response to the Early Pliocene Shoaling of the Central American Seaway. *Sci Rep* 5:12252. <https://doi.org/10.1038/srep12252>.
- Bell DB, Jung SJA, Kroon D, Lourens LJ, Hodell DA (2014) Local and regional trends in Plio-Pleistocene $\delta^{18}\text{O}$ records from benthic foraminifera. *Geochem Geophys Geosystems* 15:3304–3321. <https://doi.org/10.1002/2014GC005297>.
- Berger WH (1967) Foraminiferal ooze: solution at depths. *Science* 156(3773):383–385. <https://doi.org/10.1126/science.156.3773.383>.
- Berger WH, Bonneau MC, Parker FL (1982) Foraminifera on the deep-sea floor: lysocline and dissolution rate. *Oceanol Acta* 5:249–258.
- Betzler C, Eberli GP, Lüdmann T, Reolid J, Kroon D, Reijmer JGG, Swart PK, Wright J, Young JR, Alvarez-Zarikian C, Alonso-García M, Bialik OM, Blättler CL, Guo JA, Haffen S, Horozal S, Inoue M, Jovane L, Lanci L, Laya JC, Hui Mee AL, Nakakunim M, Nath BN, Niino K, Petruny LM, Pratiwi SD, Slagle AL, Sloss CR, Su X, Yao Z (2018) Refinement of Miocene sea level and monsoon events from the sedimentary archive of the Maldives (Indian Ocean). *Prog Earth Planet Sci* 5(5). <https://doi.org/10.1186/s40645-018-0165-x>.
- Clift PD (2017) Cenozoic sedimentary records of climate-tectonic coupling in the Western Himalaya. *Prog Earth Planet Sci* 4(39). <https://doi.org/10.1186/s40645-017-0151-8>.
- de Boer B, Lourens LJ, Van De Wal RSW (2014) PerSitent 400,000-year variability of Antarctic ice volume and the carbon cycle is revealed throughout the Plio-Pleistocene. *Nat Commun* 5:2999. <https://doi.org/10.1038/ncomms3999>.
- De Vleeschouwer D, Vahlenkamp M, Crucifix M, Pälike H (2017) Alternating Southern Northern Hemisphere climate response to astronomical forcing during the past 35 m.y. *Geology* 45:375–378. <https://doi.org/10.1130/G38663.1>.
- deMenocal PB, Bristow JF, Stein R (1992) Paleoclimatic applications of downhole logs: Pliocene-Pleistocene results from hole 798B, Sea of Japan. *Proc ODP Sci Results* 127/128(Pt. 1):337–353. <https://doi.org/10.2973/odp.proc.sr.127128-1.143.1992> College Station TX (Ocean Drilling Program).
- Drury AJ, John CM, Shevenell AE (2016) Evaluating climatic response to external radiative forcing during the Late Miocene to Early Pliocene: new perspectives from eastern equatorial Pacific (IODP U1338) and North Atlantic (ODP 982) locations. *Paleoceanography* 31:167–184. <https://doi.org/10.1002/2015PA002881>.
- Gamo T, Nakayama N, Takahata N, Sano Y, Zhang J, Yamazaki E, Taniyasu S, Yamashita N (2014) The Sea of Japan and its unique chemistry revealed by time-series observations over the last 30 years. *Monogr Environ Earth Planets* 2:1–22. <https://doi.org/10.5047/meep.2014.00201.0001>.
- Gamo T, Nozaki Y, Sakai H, Nakai T, Tsubota H (1986) Spatial and temporal variations of water characteristics in the Japan Sea bottom layer. *J Mar Res* 44:781–793. <https://doi.org/10.1357/002224086788401620>.
- Hase H, Yoon JH, Koterayama W (1999) The current structure of the Tsushima warm current along the Japanese coast. *J Oceanogr* 55:217–235. <https://doi.org/10.1023/A:1007894030095>.
- Hinnov LA (2000) New perspectives on orbitally forced stratigraphy. *Annu Rev* 28:419–475. <https://doi.org/10.1146/annurev.earth.28.1.419>.
- Hinnov LA, Hilgen FJ (2012) Cyclostratigraphy and astrochronology. In: Gradstein F, Ogg J, Ogg G, Smith D (eds) *A geologic time scale 2012*, vol 4. Elsevier, Amsterdam, pp 63–83.
- Hodell DA, Curtis JH, Siero FJ, Raymo ME (2001) Correlation of Late Miocene to Early Pliocene sequences between the Mediterranean and North Atlantic. *Paleoceanography* 16:164–178. <https://doi.org/10.1029/1999PA000487>.
- Holbourn A, Kuhnt W, Clemens S, Prell W, Anderson N (2013a) Middle to Late Miocene stepwise climate cooling: evidence from a high-resolution deep water isotope curve spanning 8 million years. *Paleoceanography* 28:688–699. <https://doi.org/10.1002/2013PA002538>.
- Holbourn A, Kuhnt W, Frank M, Haley BA (2013b) Changes in Pacific Ocean circulation following the Miocene onset of permanent Antarctic ice cover. *Earth Planet Sci Lett* 365:38–50. <https://doi.org/10.1016/j.epsl.2013.01.020>.
- Holbourn A, Kuhnt W, Schulz M, Erlenkeuser H (2005) Impacts of orbital forcing and atmosphere carbon dioxide on Miocene ice-sheet expansion. *Nature* 438:483–487. <https://doi.org/10.1038/nature04123>.
- Holbourn A, Kuhnt W, Schulz M, Flores JA, Anderson N (2007) Orbitally-paced climate evolution during the middle Miocene "Monterey" carbon-isotope excursion. *Earth Planet Sci Lett* 261:534–550. <https://doi.org/10.1016/j.epsl.2007.07.026>.
- Holbourn AE, Kuhnt W, Clemens SC, Kochhann KG, Jöhneck J, Lübbers J, Andersen N (2018) Late Miocene climate cooling and intensification of southeast Asian winter monsoon. *Nat Commun* 9(1):1584.
- Horozal S, Kim GY, Cukur D, Bahk JJ, Buchs D, Ryu BJ, Lee GH, Kim SP (2017) Sedimentary and structural evolution of the Eastern South Korea Plateau (ESKP), East China Sea (Japan Sea). *Mar Pet Geol* 85:70–88. <https://doi.org/10.1016/j.marpetgeo.2017.04.014>.
- Iijima A, Tada R (1990) Evolution of tertiary sedimentary basins of Japan in reference to opening of the Japan Sea. *J Fac Sci Univ Tokyo Section II Geol Mineral Geogr Geophys* 22:121–171.
- Irina T, Tada R, Ikehara K, Sagawa T, Karasuda A, Kurokawa S, Seki A, Lu S (2018) Construction of perfectly continuous records of physical properties for dark-light sediment sequences collected from the Japan Sea during Integrated Ocean Drilling Program Expedition 346 and their potential utilities as paleoceanographic studies. *Prog Earth Planet Sci* 5(1):23. <https://doi.org/10.1186/s40645-018-0176-7>.
- Kamikuri S, Itaki T, Motoyama I, Matsuzaki K (2017) Radiolarian biostratigraphy from Middle Miocene to Late Pleistocene in the Japan Sea. In: *Paleontol Res*. Kamikuri S, Nishi H, Motoyama A, Saito S (2004) Middle Miocene to Pleistocene radiolarians biostratigraphy in the Northwest Pacific Ocean, ODP leg 186. *Island Arc* 13:191–226. <https://doi.org/10.1111/j.1440-1738.2003.00421.x>.
- Kamikuri S, Nishi H, Motoyama I (2007) Effects of Late Neogene climatic cooling on North Pacific radiolarian assemblage and oceanographic conditions. *Paleogeogr Palaeoclimatol Palaeoecol* 249:370–392. <https://doi.org/10.1016/j.palaeo.2007.02.008>.
- Kim CH, Yoon JH (1999) A numerical modeling of the upper and the intermediate layer circulation in the East Sea. *J Oceanogr* 55:327–345. <https://doi.org/10.1023/A:1007837212219>.

- Laskar J, Robutel P, Joutel F, Gastineau M, Correia ACM, Levrard B (2004) A long-term numerical solution for the insolation quantities of the Earth. *Astron Astrophys* 428:261–285. <https://doi.org/10.1051/0004-6361:20041335>.
- Liebrand D, Beddow HM, Lourens LJ, Pälike H, Raffi I, Bohaty SM, Hilgen FJ, Saes MJM, Wilson PA, van Dijk AE, Hodell DA, Kroon D, Huck CE, Batenburg SJ (2016) Cyclostratigraphy and eccentricity tuning of the Early Oligocene through Early Miocene (30.1–17.1 Ma): *Cibicides mundulus* stable oxygen and carbon isotope records from Walvis Ridge Site 1264. *Earth Planet Sci Lett* 450:392–405. <https://doi.org/10.1016/j.epsl.2016.06.007>.
- Liebrand D, de Bakker ATM, Beddow HM, Wilson PA, Bohaty SM, Ruessink G, Pälike H, Batenburg SJ, Hilgen FJ, Hodell DA, Huck CE, Kroon D, Raffi I, Saes MJM, van Dijk AE, Lourens LJ (2017) Evolution of the Early Antarctic ice ages. *Proc Natl Acad Sci* 114:3687–3872. <https://doi.org/10.1073/pnas.1615440114>.
- Liebrand D, Lourens LJ, Hodell DA, de Boer B, van de Wal RSW, Pälike H (2011) Antarctic ice sheet and oceanographic response to eccentricity forcing during the Early Miocene. *Clim Past* 7:869–880. <https://doi.org/10.5194/cp-7-869-2011>.
- Lisiecki LE, Raymo ME (2005) A Pliocene-Pleistocene stack of 57 globally distributed benthic $\delta^{18}\text{O}$ records. *Paleoceanography* 20(1). <https://doi.org/10.1029/2004PA001071>.
- Lofi J, Voelker AHL, Ducassou E, Hernández-Molina FJ, Sierro FJ, Bahr A, Galvani A, Lourens LJ, Pardo-Igúzquiza E, Pezard P, Rodríguez-Tovar FJ, Williams T (2016) Quaternary chronostratigraphic framework and sedimentary processes for the Gulf of Cadiz and Portuguese Contourite depositional systems derived from natural gamma ray records. *Mar Geol* 377:40–57. <https://doi.org/10.1016/j.margeo.2015.12.005>.
- Lourens LJ, Sluijs A, Kroon D, Zachos JC, Thomas E, Röhl U, Bowles J, Raffi I (2005) Astronomical pacing of Late Palaeocene to Early Eocene global warming events. *Nature* 435:1083–1087. <https://doi.org/10.1038/nature03814>.
- Matsuzaki KM, Itaki T, Tada R, Kamikuri SI (2018) Paleoclimatological history of the Japan Sea over the last 9.5 million years inferred from radiolarian assemblages (IODP expedition 346 sites U1425 and U1430). *Prog Earth Planet Sci* 5(54). <https://doi.org/10.1186/s40645-018-0204-7>.
- Miller KG, Komazin MA, Browning JV, Wright JD, Mountain GS, Katz ME, Sugarman PJ, Cramer BS, Christie-Blick N, Pekar SF (2005) The Phanerozoic record of global sea-level change. *Science* 310:1293–1298. <https://doi.org/10.1126/science.1116412>.
- Miller KG, Wright JD, Fairbanks RG (1991) Unlocking the ice house: Oligocene-Miocene oxygen isotopes, eustasy, and margin erosion. *J Geophys Res* 96: 6829–6848. <https://doi.org/10.1029/90JB02015>.
- Paillard D, Labeyrie L, Yiou P (1996) Macintosh program performs time-series analysis. *EOS Trans AGU* 77:379. <https://doi.org/10.1029/96EO00259>.
- Pälike H, Norris RD, Herrle JO, Wilson PA, Coxall HK, Lear CH, Shackleton NJ, Tripathi AK, Wade BS (2006) The heartbeat of the Oligocene climate system. *Science* 314:1894–1898. <https://doi.org/10.1126/science.1133822>.
- Schulz M, Mudelsee M (2002) REDFIT: estimating red-noise spectra directly from unevenly spaced paleoclimatic time series. *Comput Geosci* 28:421–426.
- Shackleton NJ, Hall MA, Pate D (1995) Pliocene stable isotope stratigraphy of site 846. *Proc ODP Sci Res* 138:337–355.
- Tada R (1991) Origin of rhythmical bedding in middle Miocene siliceous rocks of the Onnagawa Formation, northern Japan. *J Sediment Petrol* 61:1123–1145. <https://doi.org/10.1306/D426784D-2B26-11D7-8648000102C1865D>.
- Tada R (1994) Paleoclimatological evolution of the Japan Sea. *Palaeogeogr Palaeoclimatol Palaeoecol* 108:487–508. [https://doi.org/10.1016/0031-0182\(94\)90248-8](https://doi.org/10.1016/0031-0182(94)90248-8).
- Tada R, Iijima A (1983) Petrology and diagenetic changes of Neogene siliceous rocks in northern Japan. *J Sediment Petrol* 53:911–930.
- Tada R, Iijima A (1992) Lithostratigraphy and compositional variation of Neogene hemipelagic sediments in the Japan Sea. *Proc ODP Sci Results* 127/128(Pt. 2): 1229–1260. <https://doi.org/10.2973/odp.proc.sr.127128-2.188.1992> College Station, TX (Ocean Drilling Program).
- Tada R, Irino T, Ikehara K, Karasuda A, Sugisaki S, Xuan C, Sagawa T, Itaki T, Kubota Y, Lu S, Seki A, Murray RW, Alvarez Zarkian CA, Anderson WT Jr, Bassetti M-A, Brace BJ, Clemens SC, da Costa Gurgel MH, Dickens GR, Dunlea AG, Gallagher SJ, Giosan L, Henderson ACG, Holbourn AE, Kinsley CW, Lee GS, Lee KE, Lofi J, Lopes CID, Peterson LC, et al. (2018) High-resolution and high-precision correlation of dark and light layers in the Quaternary hemipelagic sediments of the Japan Sea recovered during IODP expedition 346. *Prog Earth Planet Sci*, 5(1), 19. <https://doi.org/10.1186/s40645-018-0167-8>.
- Tada R, Murray RW, Alvarez Zarkian CA, Anderson WT Jr, Bassetti M-A, Brace BJ, Clemens SC, da Costa Gurgel MH, Dickens GR, Dunlea AG, Gallagher SJ, Giosan L, Henderson ACG, Holbourn AE, Ikehara K, Irino T, Itaki T, Karasuda A, Kinsley CW, Kubota Y, Lee GS, Lee KE, Lofi J, Lopes CID, Peterson LC, Saavedra-Pellitero M, Sagawa T, Singh RK, Sugisaki S, Toucanne S, et al. (2015a) Methods. *Proc IODP* 346: College Station, TX (Integrated Ocean Drilling Program). <https://doi.org/10.2204/iodp.proc.346.102.2015>.
- Tada R, Murray RW, Alvarez Zarkian CA, Anderson WT Jr, Bassetti M-A, Brace BJ, Clemens SC, da Costa Gurgel MH, Dickens GR, Dunlea AG, Gallagher SJ, Giosan L, Henderson ACG, Holbourn AE, Ikehara K, Irino T, Itaki T, Karasuda A, Kinsley CW, Kubota Y, Lee GS, Lee KE, Lofi J, Lopes CID, Peterson LC, Saavedra-Pellitero M, Sagawa T, Singh RK, Sugisaki S, Toucanne S, et al. (2015b) Site U1425. *Proc IODP* 346: College Station, TX (Integrated Ocean Drilling Program). <https://doi.org/10.2204/iodp.proc.346.106.2015>.
- Tada R, Murray RW, Alvarez Zarkian CA, Anderson WT Jr, Bassetti M-A, Brace BJ, Clemens SC, da Costa Gurgel MH, Dickens GR, Dunlea AG, Gallagher SJ, Giosan L, Henderson ACG, Holbourn AE, Ikehara K, Irino T, Itaki T, Karasuda A, Kinsley CW, Kubota Y, Lee GS, Lee KE, Lofi J, Lopes CID, Peterson LC, Saavedra-Pellitero M, Sagawa T, Singh RK, Sugisaki S, Toucanne S, et al. (2015c) Site U1430. *Proc IODP* 346: College Station, TX (Integrated Ocean Drilling Program). <https://doi.org/10.2204/iodp.proc.346.110.2015>.
- Tada R, Zheng H, Clift PD (2016) Evolution and variability of the Asian monsoon and its potential linkage with uplift of the Himalaya and Tibetan plateau. *Prog Earth Planet Sci* 3:4. <https://doi.org/10.1186/s40645-016-0080-y>.
- Talley LD, Lobanov V, Ponomarev V, Salyuk A, Tishchenko P, Zhabin I, Riser S (2003) Deep convection and brine rejection in the Japan Sea. *Geophys Res Lett* 30:1159. <https://doi.org/10.1029/2002GL016451>.
- Tamaki K, Suyehiro K, Allan J, Ingle JC, Pisciotto K (1992) Tectonic synthesis and implications of Japan Sea ODP drilling. *Proc ODP Sci Results* 127/128(Pt. 2): 1333–1348. <https://doi.org/10.2973/odp.proc.sr.127128-2.240.1992> College Station TX (Ocean Drilling Program).
- Tian J, Zhao Q, Wang P, Li Q, Cheng X (2008) Astronomically modulated Neogene sediment records from South China Sea. *Paleoceanography* 23: PA3210. <https://doi.org/10.1029/2007PA001552>.
- Watanabe M (1994) A tentative model for the formation of the Late Miocene submarine hiatus around the Japan Sea. *Bull Geol Surv Japan* 45:471–475.
- Westerhold T, Bickert T, Röhl U (2005) Middle to Late Miocene oxygen isotope stratigraphy of ODP site 1085 (SE Atlantic): new constraints on Miocene climate variability and sea-level fluctuations. *Palaeogeogr Palaeoclimatol Palaeoecol* 217:205–222. <https://doi.org/10.1016/j.palaeo.2004.12.001>.
- Yanagisawa Y, Akiba F (1998) Refined Neogene diatom biostratigraphy for the northwest Pacific around Japan, with an introduction of code numbers for selected diatom biohorizons. *J Geological Soc Japan* 104:395–414.
- Zachos J, Pagani M, Sloan L, Thomas E, Billups K (2001) Trends, rhythms, and aberrations in global climate 65 ma to present. *Science* 292:686–693. <https://doi.org/10.1126/science.1059412>.

Submit your manuscript to a SpringerOpen journal and benefit from:

- Convenient online submission
- Rigorous peer review
- Open access: articles freely available online
- High visibility within the field
- Retaining the copyright to your article

Submit your next manuscript at ► [springeropen.com](https://www.springeropen.com)